

# NONDESTRUCTIVE EVALUATION OF CERAMIC AND METAL MATRIX COMPOSITES FOR NASA'S HITEMP AND ENABLING PROPULSION MATERIALS PROGRAMS

Edward R. Generazio  
National Aeronautics and Space Administration  
Lewis Research Center  
Cleveland, Ohio 44135

## SUMMARY

In a preliminary study, ultrasonic, x-ray opaque and florescent dye penetrant nondestructive techniques were used to evaluate and characterize ceramic and metal matrix composites. Techniques are highlighted for identifying porosity, fiber alignment, fiber uniformity, matrix cracks, fiber fractures, unbonds or disbonds between laminae, and fiber-to-matrix bond variations. The nondestructive evaluations (NDE) were performed during processing, after processing and after thermomechanical testing. Specific examples are given for  $\text{Si}_3\text{N}_4/\text{SiC}$  (SCS-6 fiber),  $\text{FeCrAlY}/\text{Al}_2\text{O}_3$  (sapphire fiber), Ti-15-3/SiC (SCS-6 fiber) materials and  $\text{Si}_3\text{N}_4/\text{SiC}$  (SCS-6 fiber) actively cooled panel components. Results of this study indicate that the choice of the NDE tools to be used can be optimized to yield a faithful and accurate evaluation of advanced composites.

## INTRODUCTION

The next generation of commercial aircraft will incorporate advanced aerodynamic and propulsion concepts that will require materials systems to be robust at extremely high temperatures and operating loads. NASA's Advanced High Temperature Engine Materials Technology (HITEMP) Program focuses on the development of these enabling materials and structures for rotorcraft, ultrahigh bypass ratio engines for subsonic aircraft and supersonic High Speed Civil Transport (HSCT). The development of a demonstration combustor liner and nozzle for the HSCT is being supported by NASA's Enabling Propulsion Materials program (EPM). Within the EPM program, ceramic, intermetallic, and metallic matrix composites (CMC's, IMC's, and MMC's) are being screened and evaluated (refs. 1 to 4) for their use as base materials for the HSCT's combustor liner and nozzle. Nondestructive evaluation (NDE) plays an important dual role in the development of these materials and in the evaluation and certification of components before and during use. It is a challenge for nondestructive evaluation community to establish inspection (NDI), and evaluation (NDE) techniques that are accepted, reliable, and standardized for these enabling advanced composite systems.

Materials development and tailoring can be greatly accelerated by placing NDE at critical processing stages where it can play an active and important role in the development process. NDE can assist in material properties screening, materials selection, and for determining the overall quality of finished components. NDE may occur in conjunction with or separately from proof testing. The component integrity after shipping, installation and repair will also need to be addressed by NDE. Equally important is the consideration and inclusion of nondestructive inspection (NDI) requirements at the component design stage. The components must be designed so that a nondestructive inspection can be performed. Including NDI requirements in the component design will avoid many of the inspection complications, problems, and uncertainties encountered in other aerospace systems. This level of NDI may also include nonintrusive sensors that will monitor key variables that indicate the health of the component during use. Fiber and matrix cracks, delaminations, and fiber-to-matrix interface variations are material features that affect

the composite's strength and toughness, and therefore are prime candidates for quantitative nondestructive evaluation.

There are many NDE tools that can be used for evaluating materials. The choice of the tool to use for the inspection is one of the most important decisions during the inspection procedure. For example, an eddy current instrument will not be sensitive to the presence of cracks in an electrically nonconducting material. Although this is an extreme and obvious example there are numerous of these instrument-material mismatches that are more subtle and as such must be avoided. It is appropriate to establish which methods, instruments and techniques are best suited for the NDI and NDE at each stage of the combustor liner and nozzle development, certification, installation, repair and use.

This work is a preliminary study that highlights standard NDE techniques for advanced composite systems. Five accepted NDE techniques were used; ultrasonic "C" and surface wave scans, conventional and microfocus x-ray film radiography, and florescent and x-ray opaque penetrants (refs. 5 and 6). These techniques can be used to characterize fiber fractures, matrix cracks, porosity variations, delaminations, unbonds, debonds, and fiber-to-matrix interface variations. A variation on the data acquisition configuration and data analysis for a conventional c-scan system yields images of subsurface fibers and their "degree of bonding" to the matrix. This data acquisition and data analysis process extracts the subsurface reflection coefficient at the fiber-to-matrix interface from the surface reflection coefficient obtained from a standard c-scan. This Deep Reflection Coefficient Imaging (DERCI) (ref. 7) technique is in a development stage and is also shown here with its very promising preliminary results. Eddy current (ref. 5) and other more advanced techniques, such as, thermal diffusivity imaging (refs. 8 and 9), shearography (ref. 10), speckle interferometry, scanning acoustic microscopy (SAM) (ref. 11), and scanning electron acoustic microscopy (SEAM) (refs. 12 and 13), and computed aided x-ray tomography (CAT) (ref. 14) will be addressed in a separate article to be published at a later date.

The following is organized into two sections: (1) NDE for processing and quality; and (2) NDE for degradation. The goal of this work is to show how NDE tools can be used effectively to impact the processing procedures, evaluate the finished component or test piece, and evaluate the degree of degradation that occurs from use or thermomechanical testing.

## NDE FOR PROCESSING AND QUALITY

### Ceramic Matrix Composites

We begin our study with the development of a  $\text{Si}_3\text{N}_4$ /SCS-6 (ref. 15) panel that contains coolant channels (fig. 1). The actively cooled panel is made up of a monolithic, 10.0 by 10.0 cm,  $\text{Si}_3\text{N}_4$  slab that is laminated to a cross-ply composite panel  $\text{Si}_3\text{N}_4$ /SCS-6 [0-90]. The laminated panel is 0.335 cm thick. The monolithic panel has 0.05 cm wide and 0.05 cm high coolant channels. The channel walls are 0.05 cm thick. During the development of this panel the interlaminar bonding procedure is evaluated by bonding two similar but monolithic plates. The bond between planar layers may be evaluated with radiographic and through transmission, 10 MHz, ultrasonic c-scan analysis; the results are shown in figures 2 and 3, respectively. A low x-ray intensity, i.e., high x-ray attenuation, corresponds to dark region in the x-ray film positive. The dark vertical bands in the radiograph correspond to the walls of the coolant channels. The channels are uniform in shape and there are no chips, cracks or occlusions present. There are two lighter vertical bands at areas where poor reaction of the bonding material produced low densities. (A subsequent modification of the manufacturing process eliminated these poorly reacted areas.) The

ultrasonic c-scan shows these poorly reacted regions more clearly and to be somewhat larger than that observed in the radiograph. The condition of the channels can not be determined from the ultrasonic information.

Figures 4 and 5 show the radiographic and 10 MHz, ultrasonic c-scan results for a  $\text{Si}_3\text{N}_4/\text{SCS-6}$   $[0^\circ]$  panel. Severe microcracking is observed in the radiograph as short light horizontal lines. The microcracks are most visible at the walls of the coolant channels. Note that in the enlarged region of the radiograph the crack lengths are not limited to the channel wall thickness but actually are several channels wide. The short dark vertical lines scattered throughout the image each have a short horizontal dark line at their central regions. These short dark vertical regions are regions where the channel has decreased in width. The dark horizontal line at the center of each of these regions, when examined at high magnifications, has been found to be an optical illusion that occurs where the channel walls have the closest approach to each other. At the region of closest approach some channels are partially blocked by this narrowing of the channel. Several channels had adjacent walls that were of sufficient thickness that the walls were touching and apparently completely blocking the channel. The ultrasonic image reveals a considerable amount of disordered mottling in the structure. The radiograph does exhibit density variations. There is no correlation between the mottling structure in the ultrasonic c-scan image and the crack structure observed in the radiograph. This mottling is due to porosity and bond variations between the laminated layers (refs. 16 to 22).

In the previous example the fiber orientation is not easily determined. Figures 6 and 7 show the radiographic and 10 MHz, ultrasonic, c-scan images of a  $\text{Si}_3\text{N}_4/\text{SCS-6}$   $[0/90^\circ]$  composite panel that does not have coolant channels. The radiograph reveals a bowed fiber system. These bowed patterns are not actual individual bowed fibers but are x-ray "shadows" of a collection of fibers that are bowed. The shadows forming the bowed pattern are due to fiber volume density variations through the thickness and perpendicular to the x-ray film plane. This is manifestation of the Moiré effect (refs. 18 and 23) found in composite systems. The density of the system is uniform as indicated by the uniform gray level or shading in the radiograph. The dark areas in the ultrasonic image also yielded reflected ultrasonic signals that corresponded to reflections from the laminated boundary, these dark areas are regions having poor or no bond between laminated layers.

Fibers need only be well ordered and spaced uniformly in the plane of a  $\text{Si}_3\text{N}_4/\text{SCS-6}$   $[0/90]$  plate in order to yield relatively uniform radiographic and ultrasonic images (fig. 8). However, if there are any systematic variations, such as, ordered through the thickness buckling (due to processing) of the fibers (fig. 9), then the ultrasonic image will reveal this systematic fiber spacing variations. The fiber buckling can be readily observed in the photomicrograph (fig. 9) by comparing the spacing between the bottom two rows of fibers that are perpendicular to the cross section. Note that this spacing varies dramatically from center to the right edge of the sample. In this case, the fibers are forming a crude diffractive/refractive acoustic lens (fig. 9) that is observed as a bright spot in the ultrasonic image. No indication of this fiber buckling is seen in the radiograph.

A  $\text{SiC}/\text{SiC}$  (Nicalon fiber) laminated, two-dimensional, woven composite yield very complicated radiographic and 10 MHz, ultrasonic c-scan (fig. 10) images. The radiograph reveals a cross hatch pattern that varies in density. This variation may be due to density variations in the matrix material or registration variations between the woven layers. The dark circular regions that are uniformly spaced are due to local density variations that have been produced during processing. These circular density variations are also visible in the ultrasonic image. The distorted or blurry appearance of the ultrasonic images

is due to refractive and diffractive scattering (ref. 17) occurring at the rough surfaces and woven fibers. There is little additional information obtained from the 10 MHz, ultrasonic c-scan.

### Metallic Matrix Composites

During the development of potential metal matrices the processing procedures are optimized by a combination of methods. One technique developed for consolidating metallic glass powders requires the use of a molybdenum or niobium encapsulating can for hot isostatic pressing (HIP). Radiographic (fig. 11) and ultrasonic (fig. 12) imaging can be performed while the consolidated material, NbYSi is still encapsulated. The radiograph reveals an extensive amount of cracking throughout the consolidated material. Regions of increased porosity can be readily identified as light cloud-like areas in the radiograph and dark areas in the ultrasonic image. The crack density increases with an increase in porosity.

The degree of consolidation was monitored in Ti-15-3/SiC (SCS-6) fiber composites with radiographic (fig. 13) and ultrasonic imaging (fig. 14). This panel was HIPped in two steps. The second processing step has removed much of the porosity (fig. 13). A close examination of the radiograph reveals fine fiber fractures (fig. 15). The intensity of the x-rays at the fracture sites is low. This low intensity or high x-ray attenuation at the fracture sites is an indication that the matrix material has infiltrated into these fracture sites as shown in figure 15. An increase in the x-ray intensity at the fracture sites would indicate that these fracture sites contained voids. The fractures occurred during the ductile part of the HIP stage and are not due to the mismatch between the coefficients of thermal expansion of the fiber and matrix materials. The initial infiltration of the matrix into the fiber fracture sites was radiographically observed after the first HIP stage.

Composites with three phases yield complex radiographic and ultrasonic data. A Ti-15-3 plate containing unidirectional SiC (SCS-6) fibers and a molybdenum wire mat represents a simple three phase composite system. Groups of molybdenum wires can be identified in the 10 MHz, ultrasonic c-scan image (fig. 16) as faint uniformly spaced vertical lines. Here each group of mat wires act as an ultrasonic line scatter. Dark horizontal bands in the upper and lower parts of the ultrasonic image are due to the slight bunching of the horizontal SiC fibers, i.e., areas having high fiber volume density. The central region of the ultrasonic image also exhibits some horizontally oriented mottling. This mottling is due to similar fiber volume density variations except that these fiber volume density variations are not as ordered as those near the upper and lower edges of the plate. The radiograph shows both the orientation and structure of the horizontal SiC fibers and the vertical molybdenum wires that make up the mat (fig. 17). Broken, twisted, and bent molybdenum wires are easily identifiable and occur throughout the system. Fiber rich banded zones can also be identified, but not easily, in the radiograph.

Ordered or systematic changes in the fiber volume density or orientation can produce artifacts or Moiré (refs. 17 and 23) patterns in the radiographs. For example, if in one layer, the fiber spacing, S1, is slightly different from the fiber spacing, S2, in another layer, then a Moiré pattern will be observed in the radiograph. The radiograph of a copper matrix system containing tungsten wires (fig. 18) reveals broad vertical dark Moiré bands. (This is not an advanced high temperature composite material for the HITEMP or EPM programs, but it does dramatically show an artifact that occurs in all continuous fiber composites to some degree.) In addition, if the fiber layers are also off-axis from each other then the Moiré bands will also be off-axis.

## NDE FOR DEGRADATION

### Ceramic Matrix Composites

There is a wide range of degradation or failure mechanisms that can rapidly affect the properties of CMC's. The primary mechanisms that affect the properties of CMC's are erosion, interfacial oxidation, and also impact, thermal, mechanical, and acoustical stresses that initiate fiber, fiber coating, fiber-to-matrix interface, and matrix fractures. The toughness of these brittle matrix composites is strongly dependent on the character and strength of the fiber-to-matrix interface. All of the degradation mechanisms mentioned above can lead to a degradation of the interfacial shear strength. Additionally, interfacial property changes due to thermal, mechanical or chemical treatments are quite different. Thermally driven interfacial changes result in drastic changes, via loss or replacement of original interface material (refs. 24 and 25). In contrast, mechanically driven interface changes result in debonding, chipping, and movement or redistribution of the interface material (ref. 26). The following work in this section focuses on the characterization of this interface.

A new ultrasonic scanning and evaluation technique, known as Deep Reflection Coefficient Imaging (DERCI) (ref. 6), is being developed to characterize the fiber-to-matrix interface. An image generated by DERCi characterizes the reflection coefficient at the fiber-to-matrix interface. DERCi may be implemented on a conventional c-scan system by time gating and acquiring the reflected signals from the fiber-to-matrix interface. These reflected signals are superimposed, at 50 MHz, onto the reflection from the front surface of the test sample to form a signal with multiple peaks. Most often the signal reflected from the front surface is not collected but used as a trigger for collecting signals that occur at much later times, e.g., echoes from the back surface or interlaminar delaminations. However, it is this front surface signal that contains detailed information about the bonding of the fibers near the surface of the sample. There is a distinct difference between surface wave and DERCi evaluations. At a fixed frequency, surface wave evaluation interrogates the surface and near surface of the sample and the signals observed are dependent on the depth of the scatterer (fiber). In contrast, the DERCi image can interrogate deep into the structure of the composite ply. In its optimum configuration the DERCi image is independent (except for geometric diffraction corrections) of the distance between the sample and ultrasonic transducer.

A brief description of the DERCi interpretation follows. The ultrasonic reflection coefficient at the fiber-to-matrix interface is expected to decrease with an increase in bonded contact area between the SiC fiber and  $\text{Si}_3\text{N}_4$  matrix. The two extreme cases of a perfectly bonded and completely unbonded SiC fibers provide the insight for identifying the expected reflection coefficient changes. Here the acoustic impedances between the SiC and  $\text{Si}_3\text{N}_4$  are similar when compared to that for a void and  $\text{Si}_3\text{N}_4$ . If the SiC fibers are completely unbonded, then the ultrasound will see the SiC fiber region as a void (maximum impedance difference) and, therefore, will yield a maximum amount of scattering at this type of interface. If the fibers are perfectly bonded then ultrasound with wavelengths much greater than the interface thickness will pass across this interface into and through the fiber with little scattering at the interface. In terms of imaging, a well bonded fiber with its low reflection coefficient at the interface will be difficult to observe acoustically, while a poorly bonded fiber with its high reflection coefficient will be easily observed acoustically.

The interface reflection coefficient will vary uniformly with changes in the interface between the fiber and the matrix. There are many interfacial characteristics, such as, thickness, density, contact area between the fiber and matrix, and modulus, that will affect the acoustic impedance of this interface

(ref. 6). Here, we will focus on mechanical decoupling and thermally driven oxidation of the bonded contact area of the interface, and it's interrelationship with the interfacial shear strength.

A  $\text{Si}_3\text{N}_4/\text{SiC}$  [0] (SCS-6 fiber) composite was tested in tension until matrix cracking was visually observed. The specimen was then unloaded and a NDE was performed. A region of the specimen was identified that did not visually exhibit matrix cracking. A radiograph of this area reveals a uniform structure (fig. 19). A microscopic evaluation of the radiograph does not reveal the presence of any micro-cracks. However, a 50 MHz, ultrasonic DERC image (fig. 20) reveals a detailed subsurface structure. The individual subsurface fibers of the first ply can be identified as horizontal features across the image. The vertical and near vertical features are cracks in the matrix material. Note that along and near the matrix cracks there are areas in the image where the fibers appear to be clear or less blurry. The fibers in these areas have decoupled from the matrix material and in doing so have formed nearly perfect cylindrical ultrasonic scattering boundary. This rather clean boundary prohibits any secondary or blur inducing scattering of the wave that would have occurred if the ultrasound travelled into the SiC fiber (fig. 21). A florescent dye penetrant makes these matrix cracks visible under an ultraviolet light (fig. 22).

A zinc iodide x-ray opaque penetrant was used to determine the extent of the debonding of the fibers from the matrix material. Immediately after the zinc iodide is applied to the sample a radiograph is taken (fig. 23). The radiograph reveals numerous cracks as light near vertical lines. These cracks can also be identified in the DERC image (fig. 20). One hour after the initial application of penetrant the sample is radiographed again (fig. 24) in an identical fashion. The sharp crack like features have become faint and broad. This is an indication that the penetrant is slowly spreading throughout the sample. The wicking of the penetrant stopped at about one hour after it's application.

An extensive amount of ultrasonic scattering is observed in a 10 MHz, ultrasonic c-scan (fig. 25). The dark areas in the ultrasonic image correspond to the areas where cracks are observed in the DERC image.

Two identically produced specimens of  $\text{Si}_3\text{N}_4/\text{SiC}$  (SCS-6) [0] were ultrasonically evaluated using the DERC technique. The DERC images are spatially filtered with a two-dimensional high pass filter before further evaluation. This filter extracts the important spatial high frequency components (i.e., reflections from the fiber-to-matrix interface) from the reflections from porosity which are generally observed as mottling in ceramics (refs. 16 to 22 and figs. 5 and 7). The DERC results reveal similar features in both samples before heat treatment (fig. 26). The vertical features in these images are due to reflections at the subsurface fiber-to-matrix interfaces. One sample was heat treated at 600 °C for 100 hr in flowing oxygen to degrade the fiber-to-matrix interface (via oxidation) (ref. 24). This heat treatment decreased the interfacial shear strength from  $18 \pm 4$  MPa to  $0.8 \pm 0.4$  MPa (ref. 24). After heat treatment there is a marked change in the DERC image. After heat treatment the reflections from the interface are more intense so that the fibers become more visible. This change in the DERC results before and after heat treatment can be quantified. The histogram maximum of the gray scale of each of the images may be used to quantify the DERC results (fig. 27). A low value for the histogram maximum indicates that there is considerable amount of scattering at the fiber-to-matrix interfaces per unit area. A high maximum value indicates that the fibers are difficult to observe and that the image is rather bland or smooth. Ideally, if the fibers were perfectly bonded, and therefore essentially unobservable (except for the small variation in the acoustic impedance between the fiber and matrix) then the DERC images would contain predominantly one shade, 128, in the gray scale. The gray scale maximums for the untreated and heat treated specimens are

1.9 and 3.3 (arbitrary units), respectively. This corresponds to about a 75 percent change in histogram amplitudes. These values can be correlated with the respective interfacial shear strengths. If the interfacial shear strength is strongly dependent on the contact area between the fiber and matrix, then the DERC results, which are also sensitive to changes in this contact area, are images of variations in interfacial shear strength. Since the fiber and matrix acoustic impedances are not identical, then the interrelationship between the DERC results and the interfacial shear strength, which to first approximation is assumed to be a linear relationship, will contain a calibration or scale factor. The radiographs before and after the heat treatment (fig. 28) show essentially similar results.

These ultrasonic results are similar (ref. 7) to those found for a series of CMC samples (fig. 29) produced to have a wide range of interfacial bond strengths (fig. 30).

### Metallic Matrix Composites

A FeCrAlY/Al<sub>2</sub>O<sub>3</sub> [0] (single crystal sapphire fiber) composite bar was tested in tension at 300 K until failure. Fine cracks in the fibers are barely visible under magnification of the radiograph shown in figure 31. The fibers fractured far away from the test area where the sample ultimately fractured. The horizontal dark and light bands are due to changes in the fiber volume density through the thickness of the sample. This banding, even though it is not cyclic, is produced in an identical way as the Moiré patterns discussed previously. Similar bands have been found in untested samples. A 50 MHz, ultrasonic surface wave examination of the region having cracked fibers also reveals the extent and location of these cracked fibers (fig. 32). A 30 MHz, ultrasonic back echo c-scan reveals a mottled matrix material (fig. 32). This mottling is related to the original surface condition (i.e., before the grinding the surface smooth) of the sample. The mottling is most likely due to porosity variations that are dependant on the manufacturing process that creates the "as produced" rough surface. Figure 33 optically shows the "as produced" and "as ground" surface structures. All samples have "as ground" surfaces before being mechanically tested. The radiograph (fig. 31) does exhibit some mottling in the matrix. However, these variations are just barely visible.

Another FeCrAlY/AL<sub>2</sub>O<sub>3</sub> [0] (single crystal sapphire fiber) sample was tested in tension at 1100 K. The mechanical test was interrupted before the sample fractured. The light region in the x-ray (fig. 34) results correspond to an area that has thinned during the test. The same horizontal light and dark banding due to fiber volume density variations are identified. These fiber volume density variations are also easily observed in the 10 MHz, ultrasonic, through transmission c-scan (fig. 34).

### DISCUSSION AND SUMMARY

Table I provides a summary of the NDE results. This table may be used as a guide to assist in the nondestructive evaluation of ceramic, intermetallic, and metal matrix composites. Table I indicates that, by choosing the appropriate NDE technique, flaws, such as, fine fiber cracks, fiber-to-matrix interface variations, porosity, matrix cracks, interlaminar disbonds or unbonds, fiber misalignment, ply registration and orientation can be easily identified with conventional NDE techniques and existing NDE systems. In addition, NDE can further assist and guide the development of composites by providing feedback information on subsurface material features that are present at various stages of processing and degradation. The ultrasonic DERC technique has been identified as a technique for evaluating "degree of bonding"

between the fiber and matrix in ceramic matrix composites. Artifacts observed in ultrasonic and radiographic images have been observed and attributed to Moiré and fiber buckling mechanisms.



## ACKNOWLEDGEMENTS

The author would like to gratefully acknowledge all of the materials research scientists in the Materials Division, NASA Lewis Research Center that produced, provided and processed the composite materials used in this work. Without their interest and assistance this work would not have been possible. I would like to thank Dr. Rebecca A. MacKay and John W. Pickens for the Ti-15-3/SiC materials; Susan L. Draper and Darrell J. Gaydos for the FeCrAlY/ $\text{Al}_2\text{O}_3$  materials. Dr. Ramakrishna Bhatt, Andy J. Eckel, Dr. Jeffrey I. Eldridge, and Dennis S. Fox for the RBSN/SiC and SiC/SiC composites. Marc R. Freedman for the  $\text{Si}_3\text{N}_4$ /SiC actively cooled panel. Dr. Mohan G. Hebsur for the NbYSi matrix material.

## REFERENCES

1. HITEMP Review 1988: Advanced High Temperature Engine Materials Technology Program, NASA CP-10025, 1988.
2. HITEMP Review 1989: Advanced High Temperature Engine Materials Technology Program, NASA CP-10039, 1989.
3. HITEMP Review 1990: Advanced High Temperature Engine Materials Technology Program, NASA CP-10051, 1990.
4. HITEMP Review 1991: Advanced High Temperature Engine Materials Technology Program, NASA CP-10082, 1991.
5. McMaster, R.C., ed.: Nondestructive Testing Handbook. Vols. 1 and 2. American Society for Nondestructive Testing, Columbus, OH, 1959.
6. Briggs, A.: Scanning Acoustic Microscopy. Oxford Univ. Press, 1991.
7. Generazio, E.R., et al: Nondestructive Evaluation of Fiber-to-Matrix Interface and Interfacial Shear Strength. To be published as NASA TM , 1992.
8. Welch, C.S., et al.: Material Property Measurements with Post-Processed Thermal Image Data. Thermosense XII: An International Conference on Thermal Sensing and Imaging Diagnostic Applications, SPIE, Vol. 1313, SPIE, Bellingham, WA, 1990, pp. 124-133.
9. Heath, D.M., et al.: Quantitative Thermal Diffusivity Measurements of Composites. Review of Progress in Quantitative Nondestructive Evaluation, Vol. 5B: Proceedings of the Twelfth Annual Review, D.O. Thompson and D.E. Chimenti, eds., Plenum Press, New York, 1986, pp. 1125-1132.
10. Hung, Y.Y.: Shearography: A Novel and Practical Approach for Nondestructive Testing. J. Nondestr. Eval., vol. 8, no. 1, 1989, pp. 55-67.
11. Briggs, A: An Introduction to Scanning Acoustic Microscopy. Oxford Univ. Press, 1985.
12. Cargill, G.S.: Ultrasonic Imaging in Scanning Electron Microscopy. Nature, vol. 286, no. 5774, 1980, pp. 691-693.
13. Cantrell, J.H.; and Quian, M.: Scanning Electron Acoustic Microscopy of SiC Particles in Metal Matrix Composites. Mater. Sci. Eng., vol. A122, 1989, pp. 47-52.
14. Martz, H.E., et al.: Nuclear-Spectroscopy-Based, First-Generation, Computerized Tomography Scanners. IEEE Trans. Nucl. Sci., vol. 38, no. 2, Apr. 1991, pp. 623-635.
15. SCS-6 SiC Fiber. Textron Specialty Materials, Lowell, MA.
16. Generazio, E.R.: Ultrasonic and Radiographic Evaluation of Advanced Aerospace Materials: Ceramic Composites. NASA TM-102540, 1990.

17. Generazio, E.R.: Theory and Experimental Technique for Nondestructive Evaluation of Ceramic Composites. NASA TM-102561, 1990.
18. Generazio, E.R.; and Swickard, S.M.: Ultrasonic and Radiographic Evaluation of Advanced Aerospace Materials: Ceramic Composites. HITEMP Review 1990: Advanced High Temperature Engine Materials Technology Program, NASA CP-10051, 1990, pp. 65-1, 65-7.
19. Generazio, E.R.; Roth D.J.; and Baaklini, G.Y.: Acoustic Imaging of Subtle Porosity Variations in Ceramics. Mater. Eval., vol. 46, no. 10, Sept. 1988, pp. 1338-1343.
20. Generazio, E.R., Roth; D.J.; and Stang, D.B.: Ultrasonic Imaging of Porosity Variations Produced During Sintering. J. Am. Ceram. Soc., vol 72, no. 7, July 1989, pp. 1282-1285.
21. Generazio, E.R.; Stang, D.B.; and Roth, D.J.: Dynamic Porosity Variations in Ceramics. NASA TM-101340, 1988.
22. Generazio, E.R.; Roth, D.J.; and Baaklini, G.Y.: Imaging Subtle Microstructural Variations in Ceramics with Precision Ultrasonic Velocity and Attenuation Measurements. NASA TM-100129, 1987.
23. Biberman, L.M.: Perception of Displayed Information. Ch. 7. Plenum Press, New York, 1973.
24. Bhatt, R.: Influence of Interfacial Shear Strength on the Mechanical Properties of SiC Fiber Reinforced Reaction-Bonded Silicon Nitride Matrix Composites. NASA TM-102462, 1990.
25. Bhatt, H.; Donaldson, K.Y.; and Hasselman, D.P.H.: Role of the Interfacial Barrier in the Effective Thermal Diffusivity/Conductivity of SiC-Fiber-Reinforced Reaction Bonded Silicon Nitride. J. Am. Ceram. Soc., vol. 73, no. 2, 1990, pp. 312-316.
26. Eldridge, J.I.; and Honey, F.S.: Characterization of Interfacial Failure in SiC Reinforced  $\text{Si}_3\text{N}_4$  Matrix Composite Material by Both Fiber Push-out Testing and Auger Electron Spectroscopy, J. Vac. Sci. Technol., vol. A8, no. 3, May/June 1990, pp. 2101-2106.
27. Baaklini, G.Y.; and Bhatt, R.T.: Preliminary Monitoring of Damage Accumulation in SiC/RBSN. HITEMP Review 1992: Advanced High Temperature Engine Materials Technology Program, NASA CP-10082, pp. 54-1 - 54-13.

TABLE I

	CMC	MMC
Matrix cracks	DERCI, FP	X, UC, FP, XP <sup>a</sup>
Fiber fractures	X <sup>b</sup>	US, X <sup>b,c</sup>
Delaminations	UC, XP	No samples with delaminations
Porosity	X, UC	X, UC
Fiber-to-matrix interface variations	DERCI, US	UC, APSS <sup>d</sup>
Fiber bunching, and layup registration	X	UC, X
Fiber alignment	X	X, UC
Fiber through-the-thickness bucking	UC	Not explicitly observed
APSS    Angular power spectrum scanning DERCI   Deep reflection coefficient imaging FP       Fluorescent penetrant UC       Ultrasonic c-scan US       Ultrasonic surface wave X        X-ray (conventional/microfocus) XP       X-ray opaque penetrant		

<sup>a</sup>Penetrants are used routinely for locating surface breaking cracks in metals (ref. 5).

<sup>b</sup>If the fracture planes are parallel direction of travel of the x-ray photons, then these may be observable when the fiber crack is widened (ref. 27).

<sup>c</sup>In a recent separate unpublished study, fractured fibers in FeCrAlY/Al<sub>2</sub>O<sub>3</sub> (sapphire) composites were unobservable using conventional radiography. This is believed to be due to the complex fracture structure and x-ray absorption properties of sapphire.

<sup>d</sup>Ultrasonic through transmission and back-echo c-scans, and angular power spectrum scanning (APSS; ref. 17), have been used to identify stress relaxation and fiber ratcheting in heat treated, thermal cycled MMC's. However, the physical scattering mechanism responsible for the interrelationship is not well understood at this time.

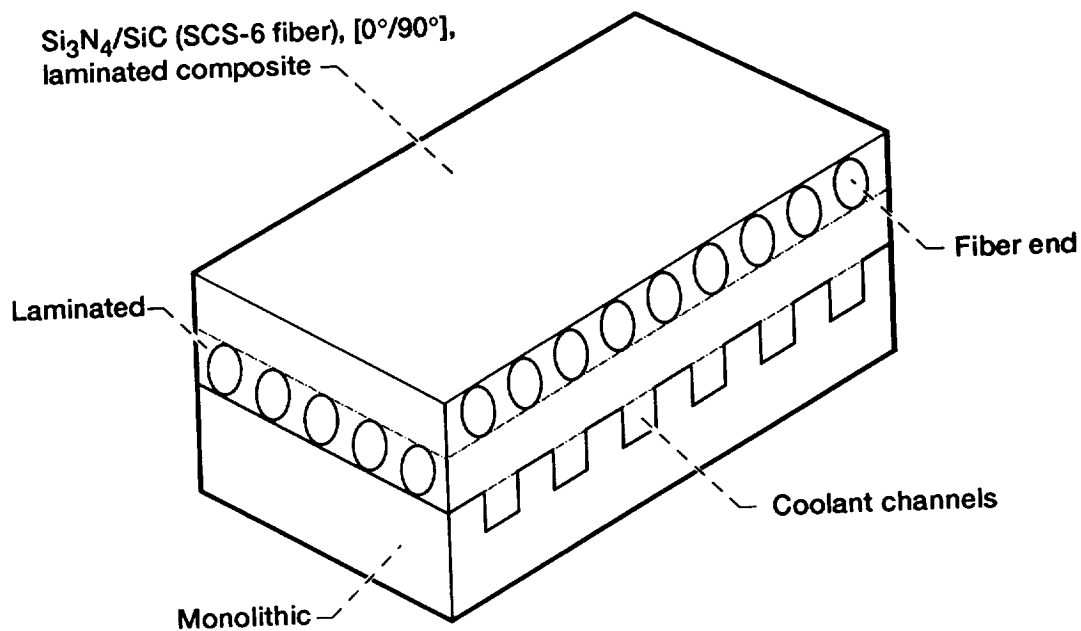


Figure 1.—Schematic diagram showing structure of composite, actively cooled panel.

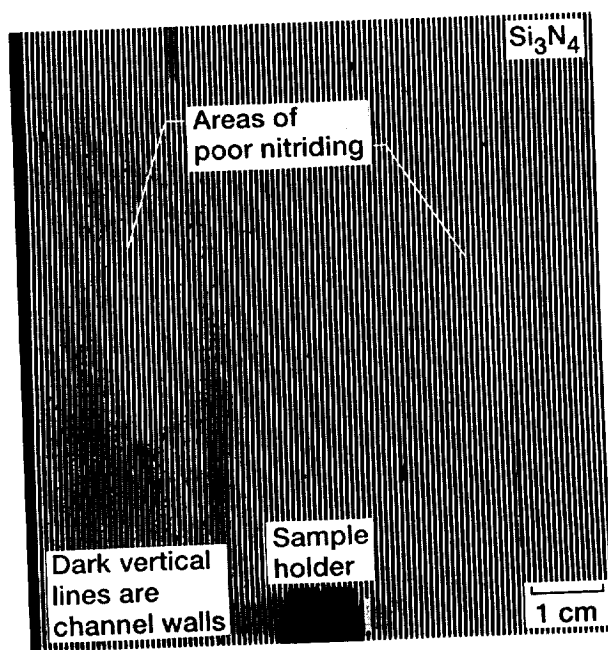


Figure 2.—Radiograph of monolithic Si<sub>3</sub>N<sub>4</sub>, actively cooled panel.

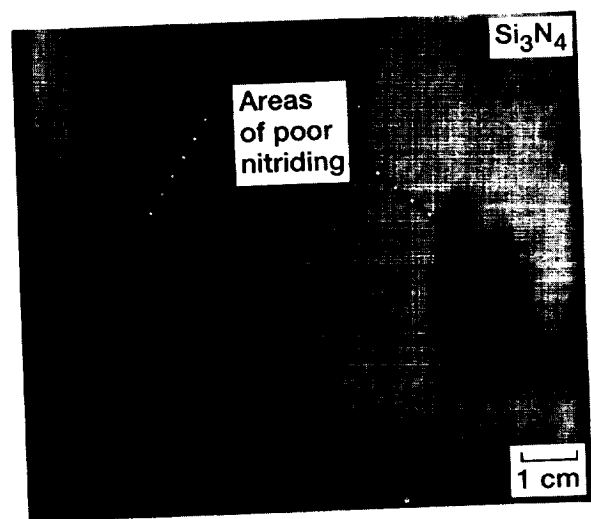


Figure 3.—Ultrasonic, 10 MHz, through transmission c-scan of monolithic Si<sub>3</sub>N<sub>4</sub>, actively cooled panel.

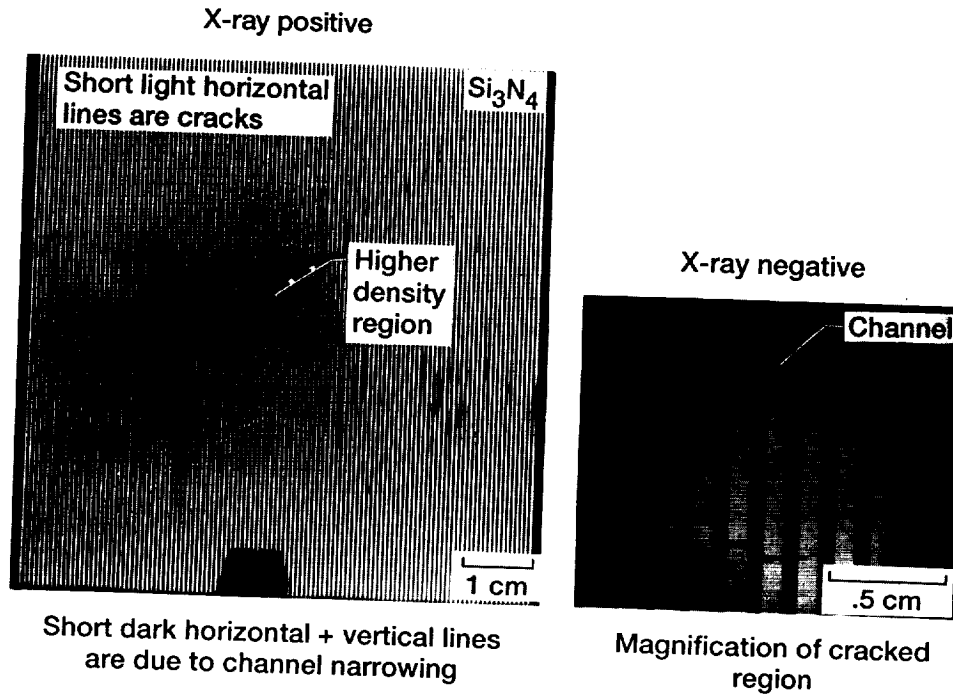


Figure 4.—Radiographs of  $\text{Si}_3\text{N}_4$ /SCS-6 [0 degree] actively cooled panel.

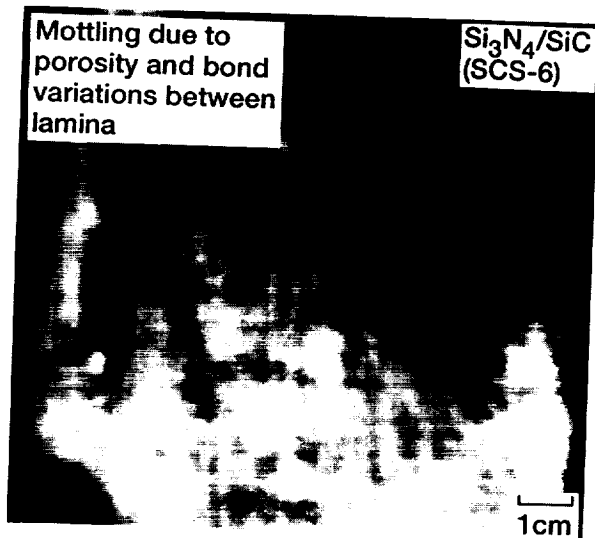


Figure 5.—Ultrasonic, 10 MHz through transmission c-scan of  $\text{Si}_3\text{N}_4$ /SiC SCS-6 [0 degree] actively coolant panel.

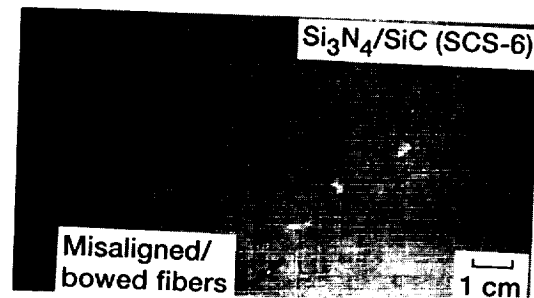


Figure 6.—Radiograph of  $\text{Si}_3\text{N}_4$ /SiC SCS-6 [0-90 degree] panel.

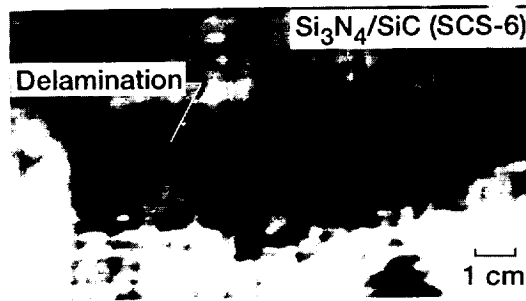


Figure 7.—Ultrasonic, 10 MHz, through transmission c-scan of  $\text{Si}_3\text{N}_4/\text{SiC}$  SCS-6 [0-90 degree] panel.

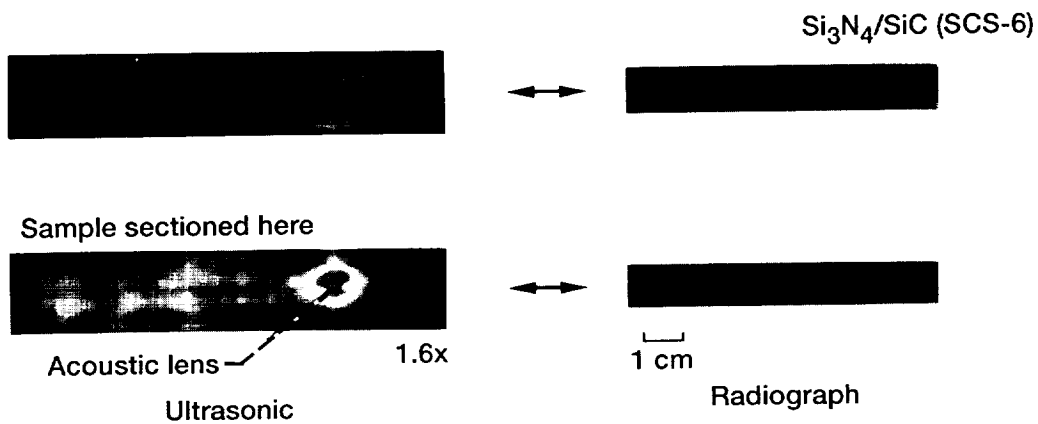


Figure 8.—Ultrasonic, 10 MHz, through transmission c-scan and radiographs of similarly produced  $\text{Si}_3\text{N}_4/\text{SiC}$  SCS-6 [0-90 degree], test bars.

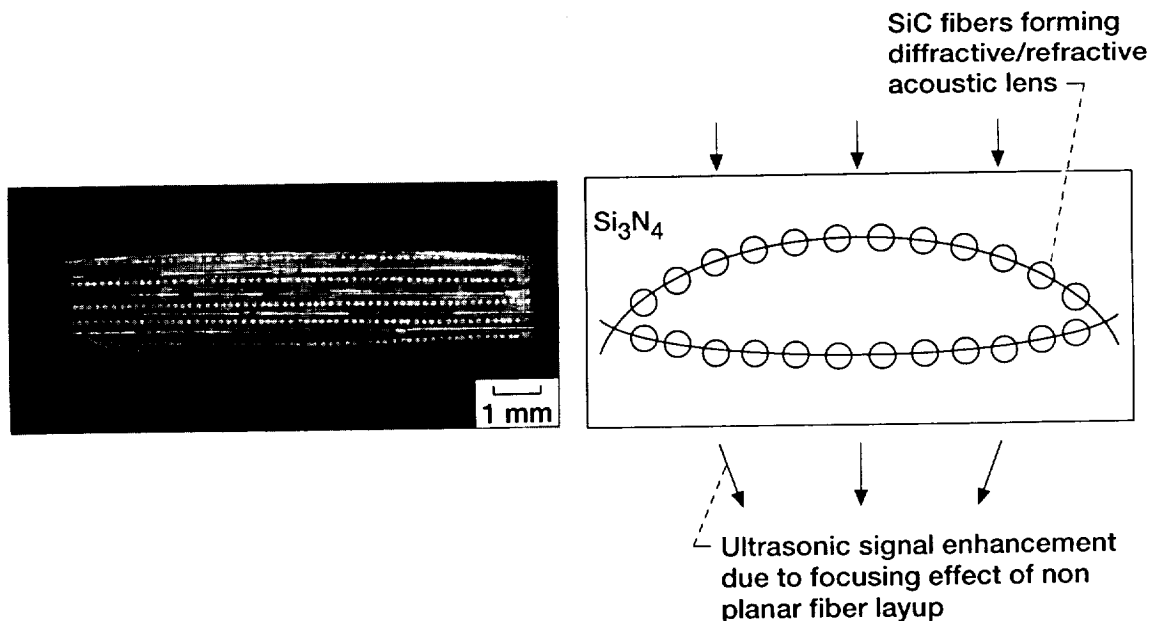


Figure 9.—Cross-section of  $\text{Si}_3\text{N}_4/\text{SiC}$  SCS-6 [0-90 degree] test bar at region showing large ultrasonic transmission.

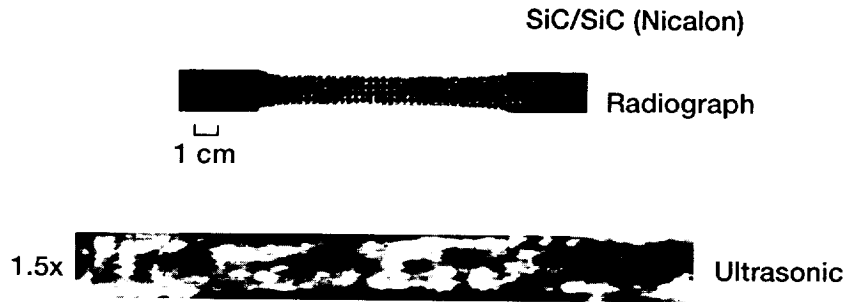


Figure 10.—Ultrasonic, 10 MHz through transmission c-scan and radiograph of SiC/SiC (Nicalon) woven laminated composite.

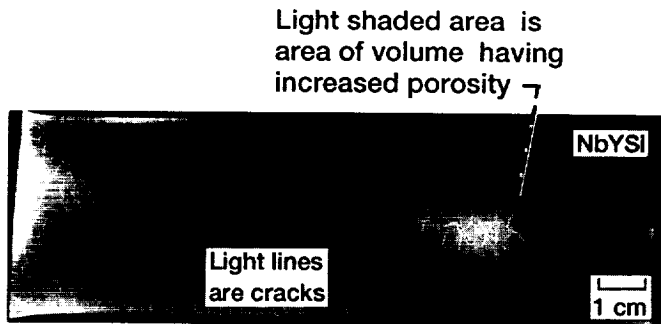


Figure 11.—Radiograph of encapsulated NbYSi matrix material.

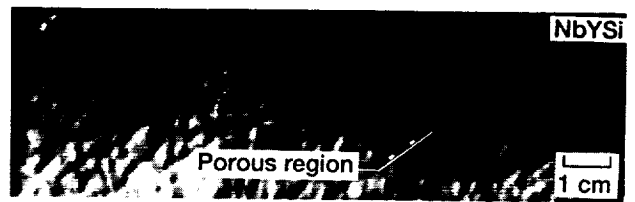


Figure 12.—Ultrasonic, 10 MHz, through transmission c-scan of encapsulated NbYSi matrix material.

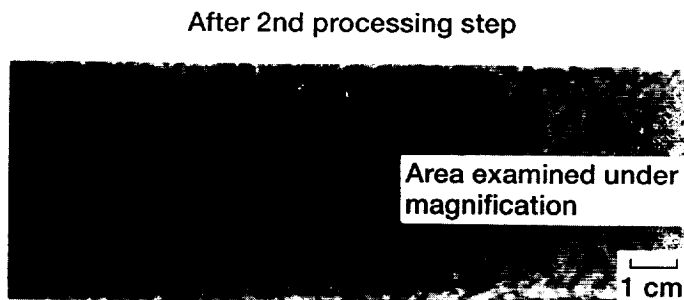
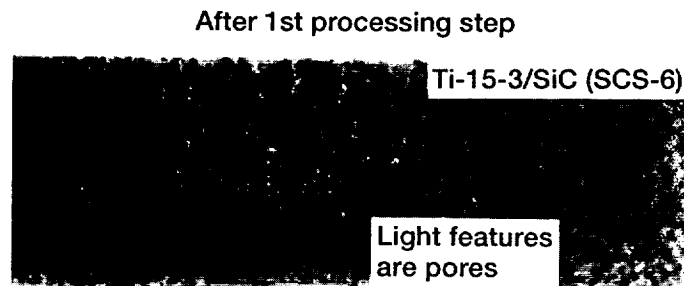


Figure 13.—Radiographs of Ti-15-3/SiC (SCS-6) composites after first and second processing steps.



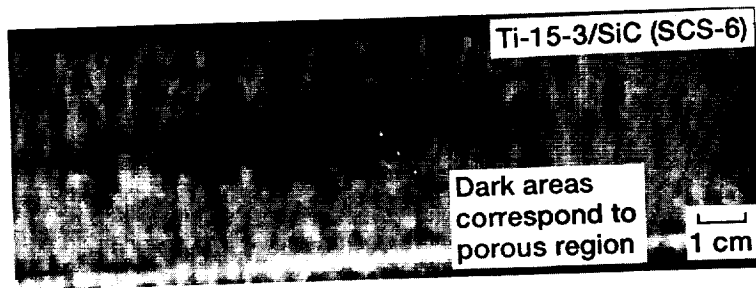


Figure 14.—Ultrasonic, 10 MHz, through transmission c-scan of Ti-15-3/SiC (SCS-6) composite after the first processing step.

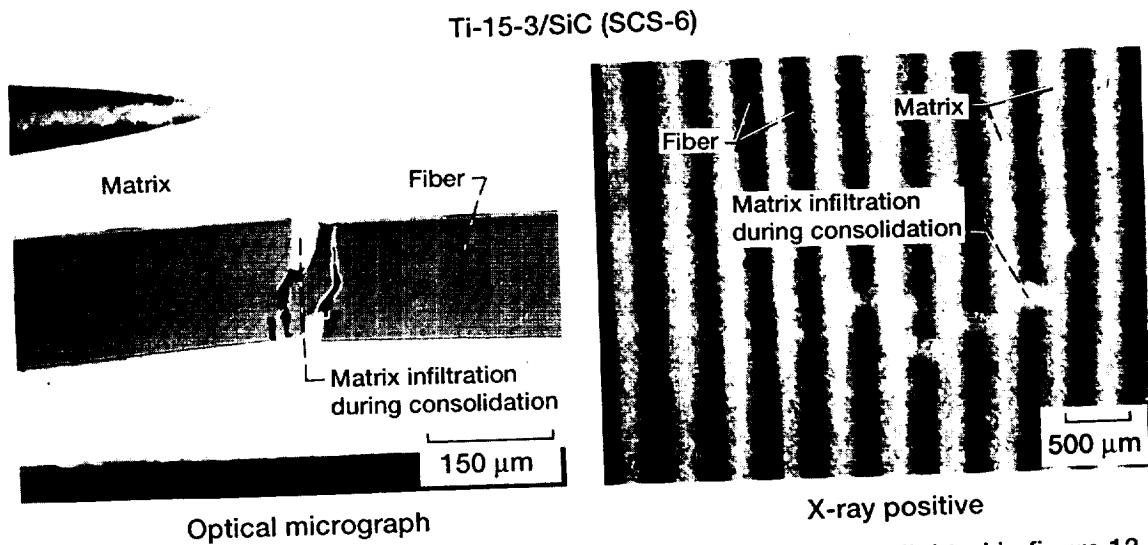


Figure 15.—Metallograph and enlarged x-ray positive of region highlighted in figure 13.

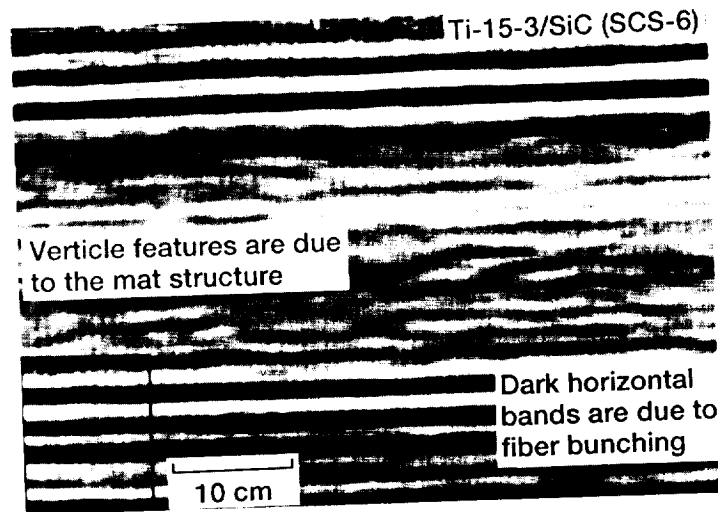


Figure 16.—Ultrasonic, 10 MHz, through transmission c-scan of Ti-15-3/SiC (SCS-6) composite.

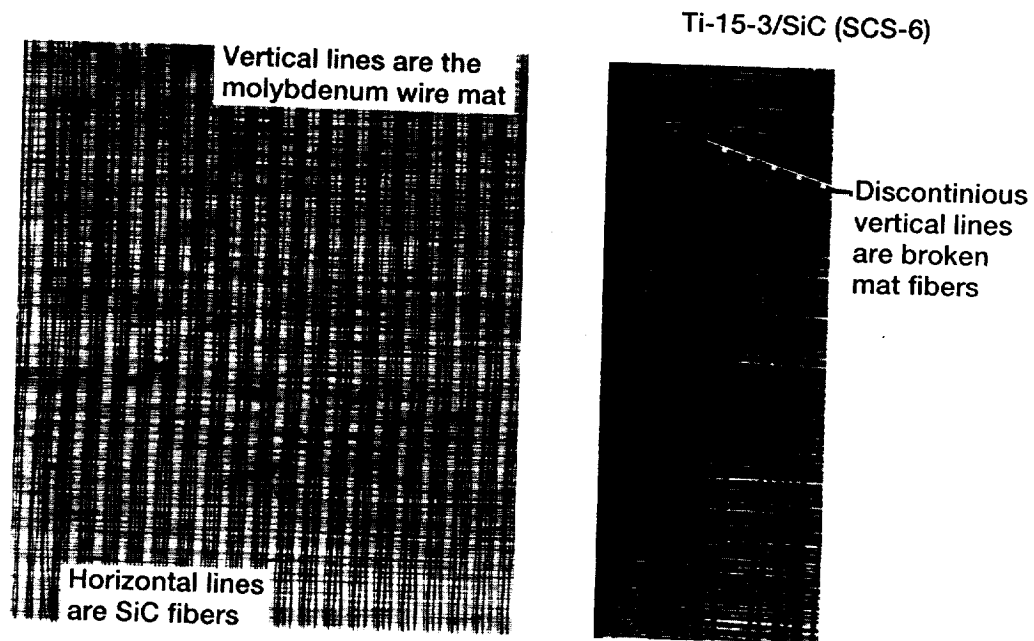


Figure 17.—Radiograph of highlighted region in figure 16.

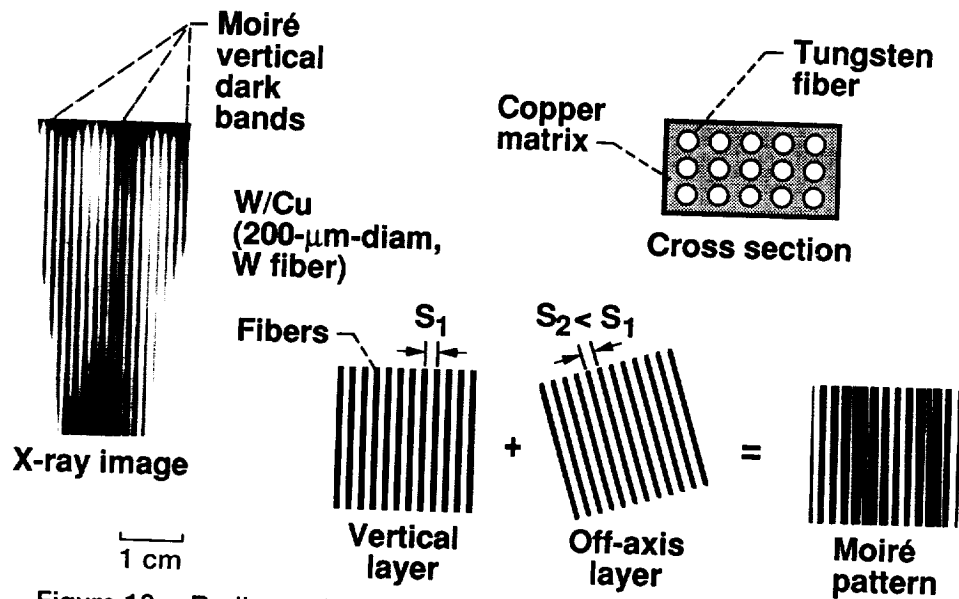
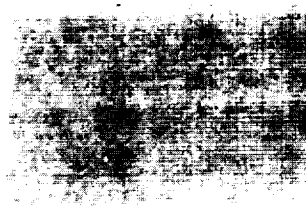


Figure 18.—Radiograph and illustrations showing Moiré effect in W/Cu composite.

$\text{Si}_3\text{N}_4/\text{SiC}$  (SCS-6)



1 cm

Figure 19.—Radiographed section of  $\text{Si}_3\text{N}_4/\text{SiC}$  SCS-6 [0] RBSN tensile test bar.

$\text{Si}_3\text{N}_4/\text{SiC}$  (SCS-6)

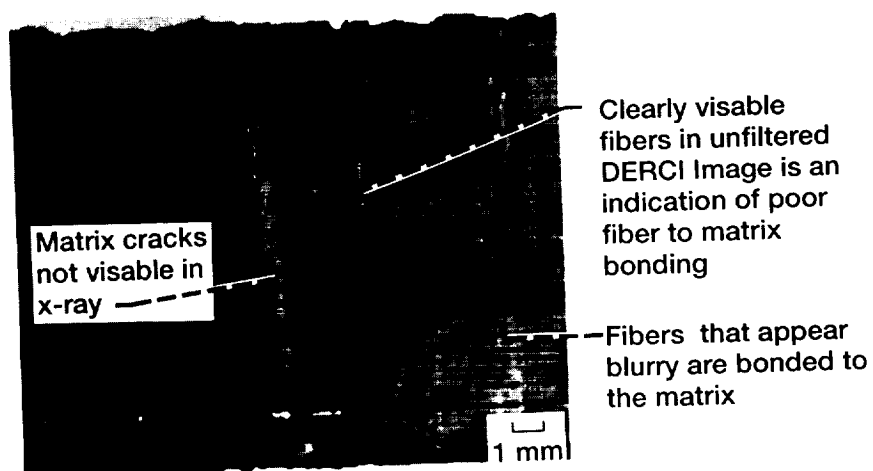


Figure 20.—Ultrasonic DERCi unfiltered image at 50 MHz of section of  $\text{Si}_3\text{N}_4/\text{SiC}$  SCS-6 [0] RBSN tensile test bar.

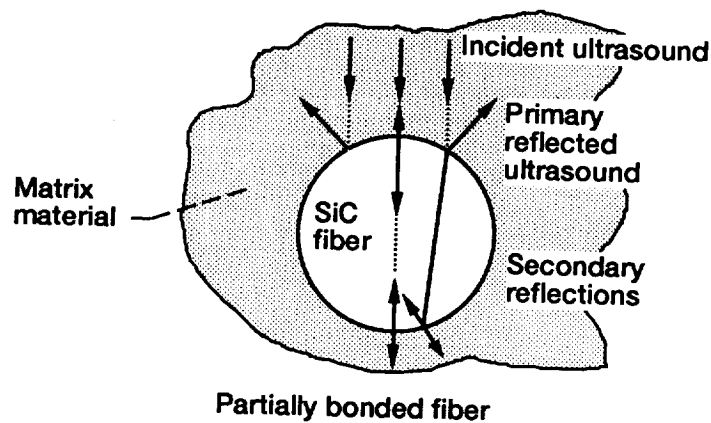
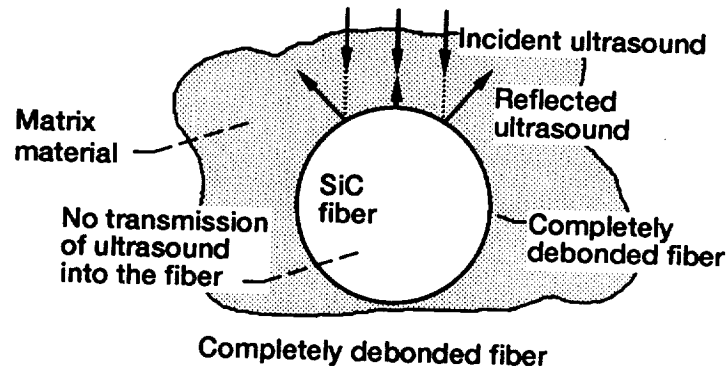


Figure 21.—Schematic diagrams indicating possible source of secondary image blurring scattering.

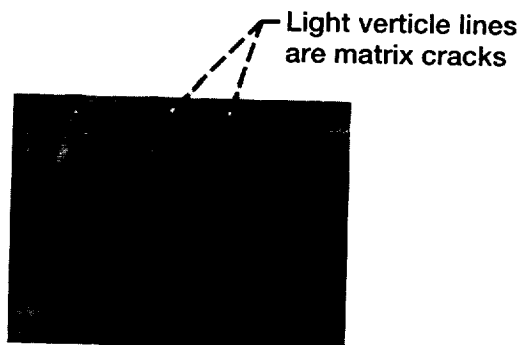


Figure 22.—Fluorescent penetrant image of section of  $\text{Si}_3\text{N}_4/\text{SiC}$  SCS-6 [0] RBSN tensile test bar.

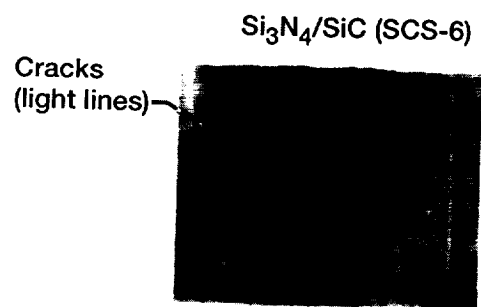


Figure 23.—Radiograph of section of  $\text{Si}_3\text{N}_4/\text{SiC}$  SCS-6 [0], RBSN tensile test bar immediately after application of zinc iodide penetrant.

ORIGINAL PAGE  
BLACK AND WHITE PHOTOGRAPH

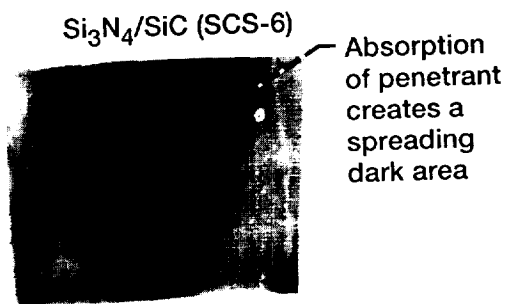


Figure 24.—Radiograph of section of  $\text{Si}_3\text{N}_4/\text{SiC}$  SCS-6 [0] RBSN tensile test bar one hour after application of zinc iodide dye penetrant.

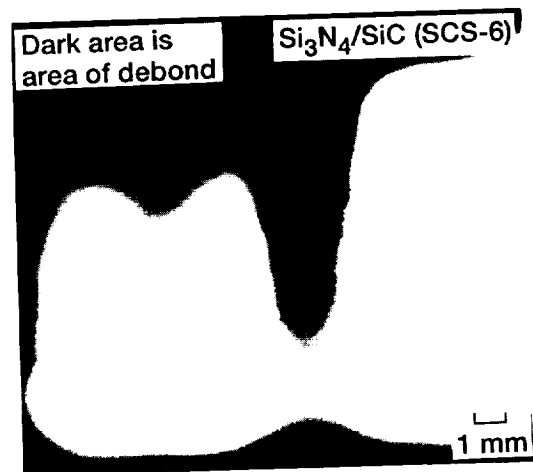


Figure 25.—Ultrasonic, 10 MHz, through transmission c-scan of section of  $\text{Si}_3\text{N}_4/\text{SiC}$  SCS-6 [0] RBSN tensile test bar.

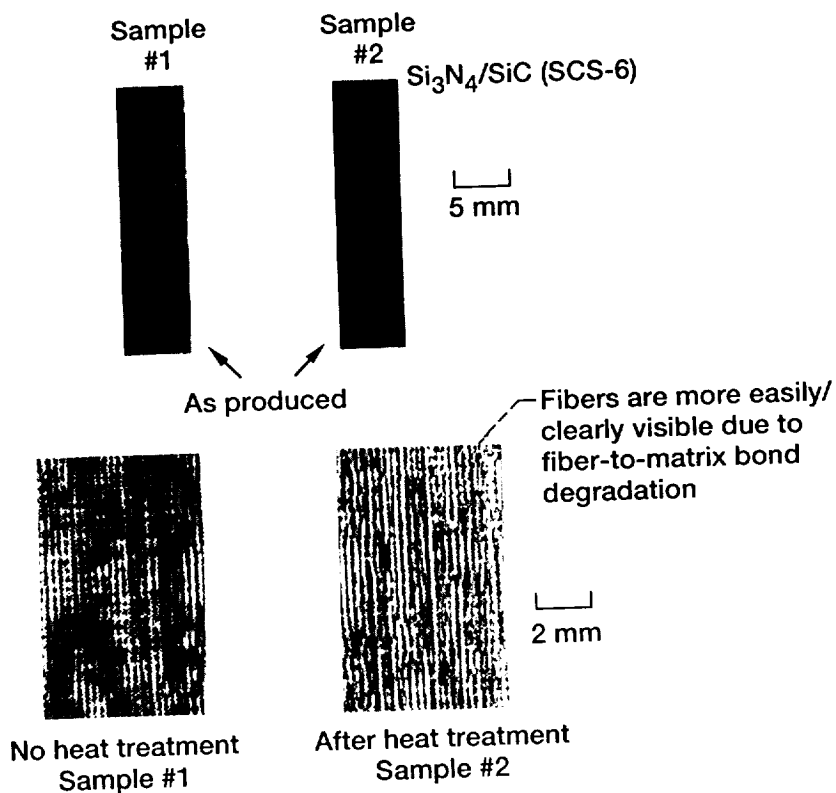


Figure 26.—DERIC images of  $\text{Si}_3\text{N}_4/\text{SiC}$  SCS-6 [0] RBSN at 50 MHz before and after heat treatment.

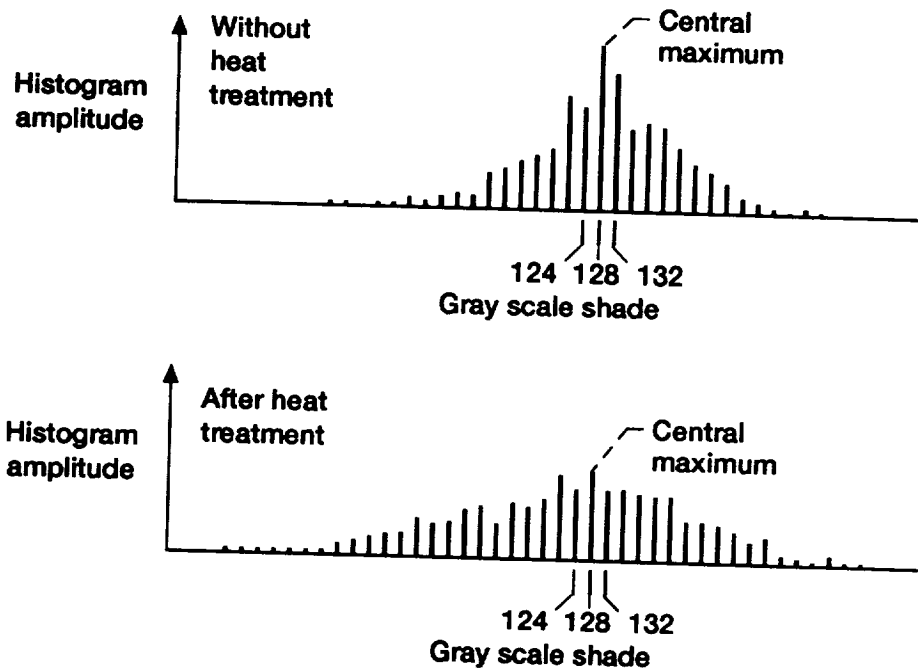


Figure 27.—Histograms of DERCI images of  $\text{Si}_3\text{N}_4/\text{SiC}$  SCS-6 [0] RBSN samples before and after heat treatment.

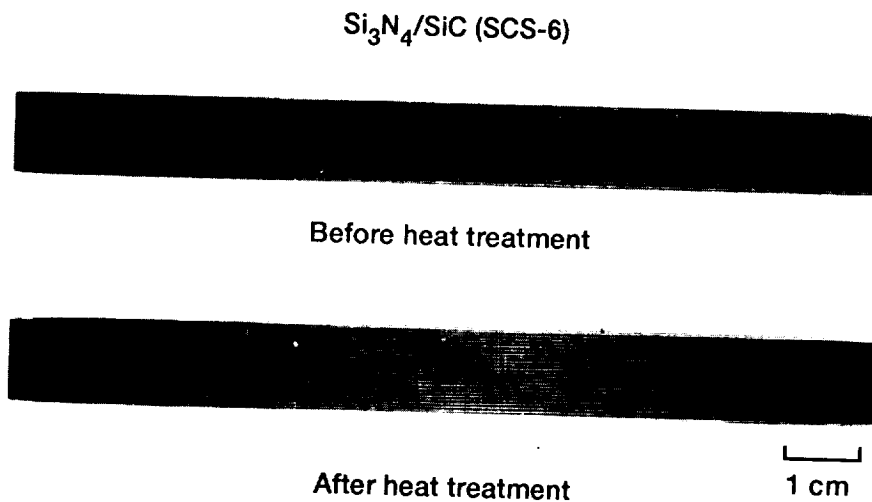


Figure 28.—Radiographs of  $\text{Si}_3\text{N}_4/\text{SiC}$  SCS-6 [0] RBSN sample #2 before and after heat treatment.

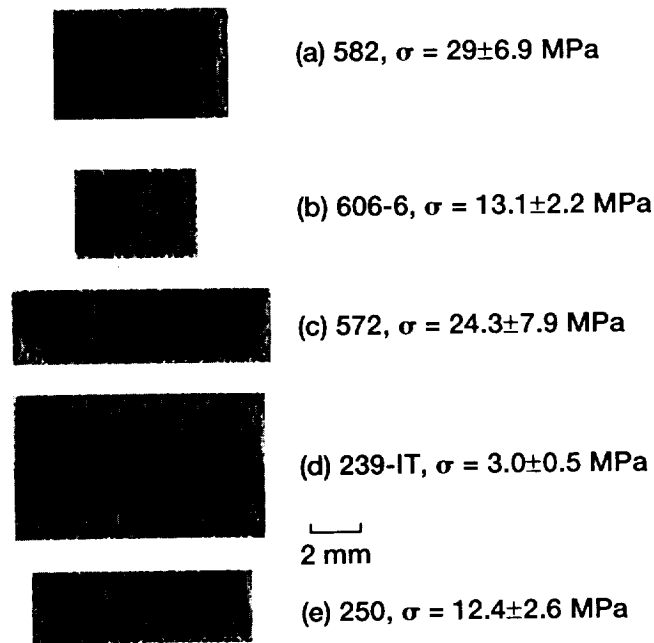


Figure 29.—DERCI images of  $\text{Si}_3\text{N}_4/\text{SiC}$  SCS-6 [0] RBSN samples having a range of interfacial shear strengths.

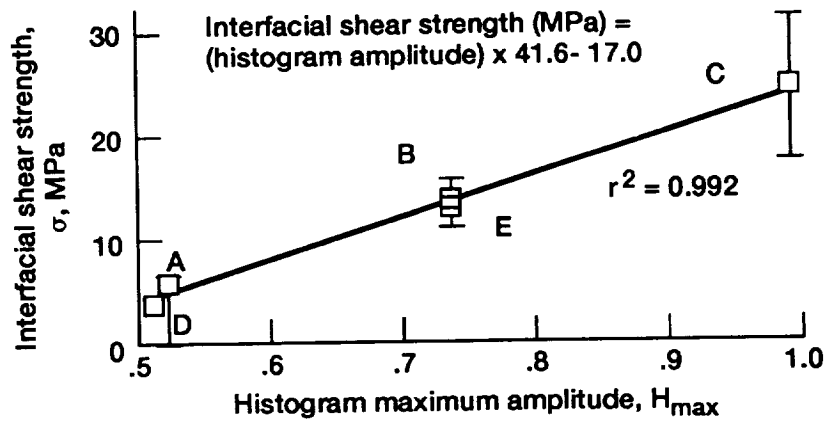


Figure 30.—Histogram maximum amplitude versus interfacial shear strength for the  $\text{Si}_3\text{N}_4/\text{SiC}$  SCS-6 [0] RBSN samples.

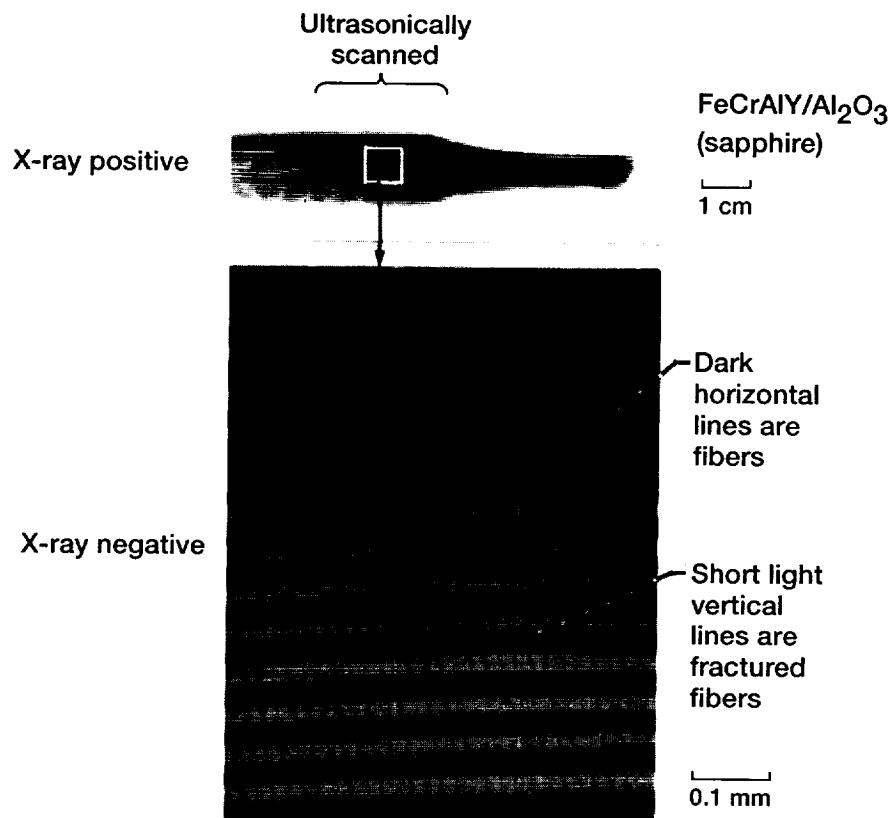


Figure 31.—Radiograph and radiographic enlargement of FeCrAlY/Al<sub>2</sub>O<sub>3</sub> (sapphire fiber) composite.

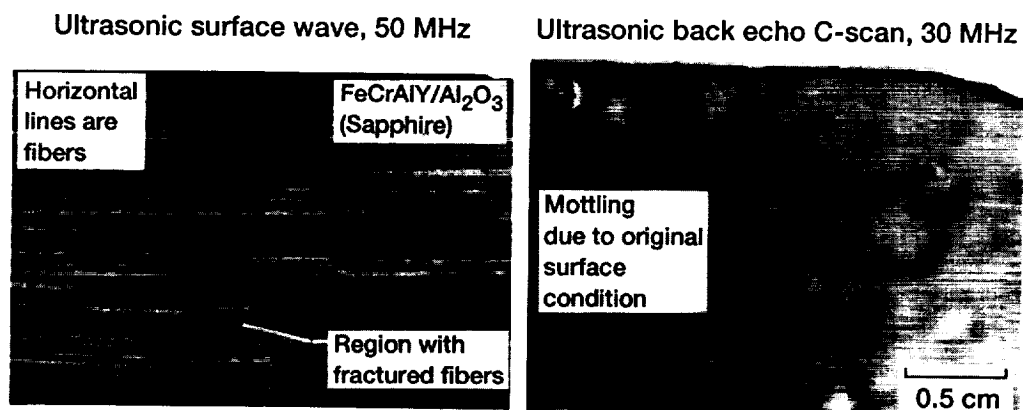


Figure 32.—Ultrasonic surface wave and back echo images of FeCrAlY/Al<sub>2</sub>O<sub>3</sub> (sapphire fiber) composite.



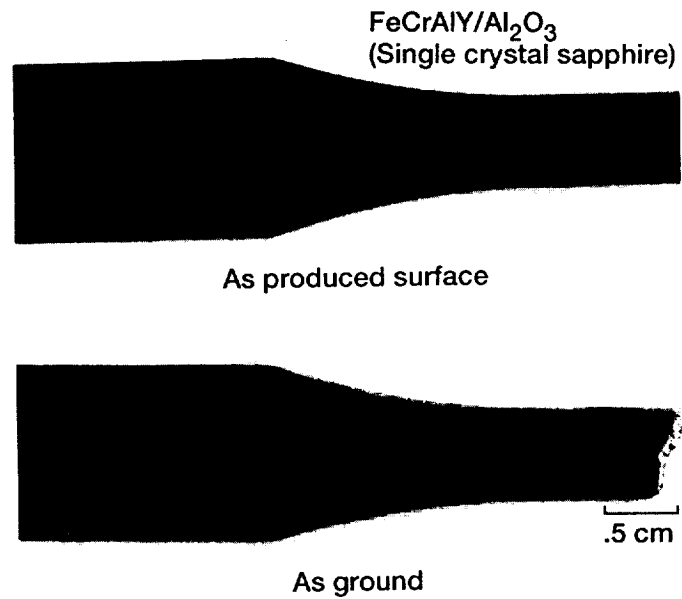


Figure 33.—Optical images of "as produced" and "as ground"  $\text{FeCrAlY/Al}_2\text{O}_3$  (sapphire fiber) composite.

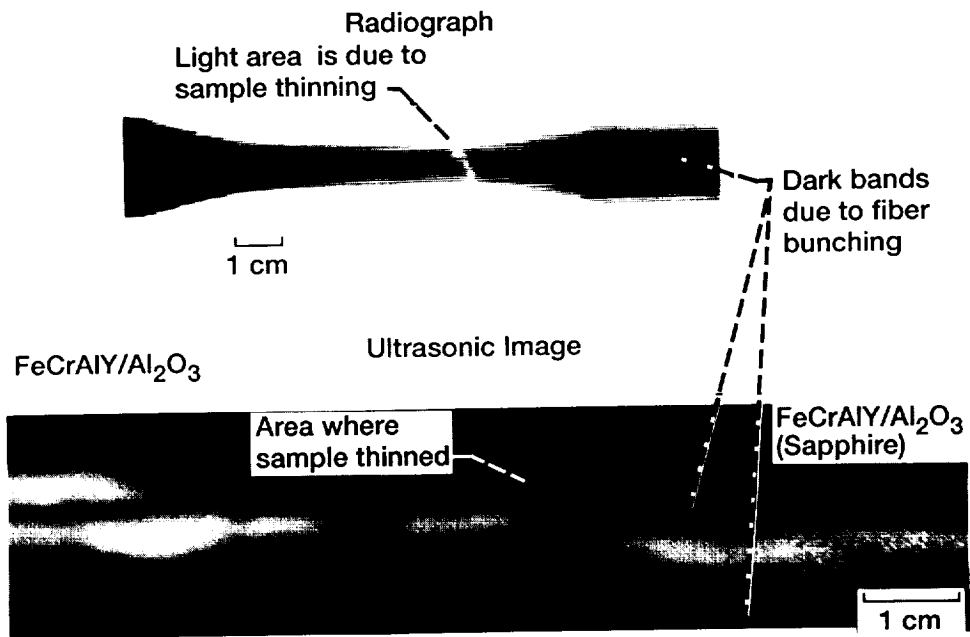


Figure 34.—Ultrasonic, 10 MHz, through transmission c-scan and radiograph of  $\text{FeCrAlY/Al}_2\text{O}_3$  (sapphire fiber) composite tensile test bar.





REPORT DOCUMENTATION PAGE			Form Approved OMB No. 0704-0188	
Public reporting burden for this collection of information is estimated to average 1 hour per response, including the time for reviewing instructions, searching existing data sources, gathering and maintaining the data needed, and completing and reviewing the collection of information. Send comments regarding this burden estimate or any other aspect of this collection of information, including suggestions for reducing this burden, to Washington Headquarters Services, Directorate for Information Operations and Reports, 1215 Jefferson Davis Highway, Suite 1204, Arlington, VA 22202-4302, and to the Office of Management and Budget, Paperwork Reduction Project (0704-0188), Washington, DC 20503.				
1. AGENCY USE ONLY (Leave blank)	2. REPORT DATE August 1992	3. REPORT TYPE AND DATES COVERED Technical Memorandum		
4. TITLE AND SUBTITLE Nondestructive Evaluation of Ceramic and Metal Matrix Composites for NASA's HITEMP and Enabling Propulsion Materials Programs		5. FUNDING NUMBERS  WU-510-01-50		
6. AUTHOR(S) Edward R. Generazio				
7. PERFORMING ORGANIZATION NAME(S) AND ADDRESS(ES)  National Aeronautics and Space Administration Lewis Research Center Cleveland, Ohio 44135-3191		8. PERFORMING ORGANIZATION REPORT NUMBER  E-7238		
9. SPONSORING/MONITORING AGENCY NAMES(S) AND ADDRESS(ES)  National Aeronautics and Space Administration Washington, D.C. 20546-0001		10. SPONSORING/MONITORING AGENCY REPORT NUMBER  NASA TM-105807		
11. SUPPLEMENTARY NOTES Portions of this paper were presented at the 16th Annual Conference on Composites, Materials, and Structures, Cocoa Beach, Florida, January 12-15, 1992. Edward R. Generazio, Lewis Research Center. Responsible person, Edward R. Generazio, (216) 433-6018.				
12a. DISTRIBUTION/AVAILABILITY STATEMENT  Unclassified - Unlimited Subject Category 38			12b. DISTRIBUTION CODE	
13. ABSTRACT (Maximum 200 words) In a preliminary study, ultrasonic, x-ray opaque and florescent dye penetrants techniques were used to evaluate and characterize ceramic and metal matrix composites. Techniques are highlighted for identifying porosity, fiber alignment, fiber uniformity, matrix cracks, fiber fractures, unbonds or disbonds between laminae and fiber-to-matrix bond variations. The nondestructive evaluations (NDE) were performed during processing and after thermomechanical testing. Specific examples are given for Si3N4/SiC (SCS-6 fiber), FeCrAlY/Al2O3 fibers, Ti-15-3/SiC (SCS-6 fiber) materials and Si3N4/SiC (SCS-6 fiber) actively cooled panel components. Results of this study indicate that the choice of the NDE tools to be used can be optimized to yield a faithful and accurate evaluation of advanced composites.				
14. SUBJECT TERMS Nondestructive tests; Metal matrix composites; Composite materials; High temperature materials; Ultrasonic flow detection; X-ray radiography; Surface waves; Ceramic matrix composites			15. NUMBER OF PAGES 26	
			16. PRICE CODE A03	
17. SECURITY CLASSIFICATION OF REPORT Unclassified	18. SECURITY CLASSIFICATION OF THIS PAGE Unclassified	19. SECURITY CLASSIFICATION OF ABSTRACT Unclassified	20. LIMITATION OF ABSTRACT	